Meandering-driven flapping of a flexible flag in a turbulent free-surface water jet

M. Sollevanti[1,*], G.P. Romano[1]

1: Dept. of Mechanical and Aerospace Engineering, University "La Sapienza", Rome, Italy
*Corresponding author: matteo.sollevanti@uniroma1.it

Keywords: Fluid-structure interaction, Flag-flapping, PIV processing.

ABSTRACT

In this work, we study the interaction and coupled dynamics between a turbulent water jet and a light, flexible Mylar flag. Since the classical self-sustained flag flutter is not easily induced for low-inertia flags immersed in water jets, due to the additional stabilizing contributions of viscous effects, we instead explored the possibility of triggering flag oscillation and flapping through an externally imposed flow unsteadiness. Unlike previous approaches based on vortex shedding in the wake of bluff bodies, here the forcing mechanism is provided by the jet's intrinsic meandering instability. In fact, once sufficiently developed, the meandering motion exhibits characteristic frequencies that are relatively stable along the streamwise direction and can be tuned through the inlet flow rate, making it a suitable candidate for imposing organized oscillations on flexible structures. Our experiments show that, in this way, flapping is accessible, also in water, at very low velocities, and that the flag's oscillations are strongly synchronized with the meandering dynamics of the jet. The dominant frequencies extracted from the flag motion match those measured in the free jet at the corresponding flow rates, while the amplitude of the flag oscillation increases along the flag length, indicating a progressive development of the deformation from the leading edge toward the trailing edge. This interpretation is further supported by the POD analysis, which shows that the flag response is dominated by a small number of coherent modes, whereas the free jet velocity field retains a broader modal content. Despite this difference, the dominant temporal and convective scales of the flag and of the jet remain close, confirming that the flag behaves as a selective structural filter of the turbulent forcing imposed by the meandering jet.

1. Introduction

The dynamics of flexible structures immersed in fluid flows represent a major challenge in fluid structure interaction, with flag flapping providing a canonical and extensively studied example, owing to its ubiquity in daily life, relevance in certain industrial applications (Watanabe et al., 2002; Chang & Moretti, 2002), and potential for small-scale energy harvesting (Allen & Smits, 2001; Wang et al., 2021). This study investigates thin, flexible flags immersed in turbulent water jets to determine whether controlled flapping frequencies can be achieved at low flow velocity. Extensive

experimental, theoretical, and numerical studies over recent decades (Taneda, 1968; Zhang et al., 2000; Shelley et al., 2005; Eloy et al., 2007, 2008; Watanabe et al., 2002; Connell & Yue, 2007) have established that a flexible flag aligned with an incoming flow can transition from a steady stretched state to periodic limit-cycle flapping and ultimately to chaotic flapping. This behavior depends on the combination of three non-dimensional parameters: the Reynolds number, the mass ratio, and the bending rigidity:

$$Re = \frac{UL}{\nu}, S = \frac{m_L}{\rho_f bL}, K_b = \frac{EI}{\rho_f U^2 L^3} \tag{1}$$

Where L is the length of the flag, $m_L = \rho_L bh$ is its mass per unit length, b its height (and therefore the height of the fluid layer interacting with the flag), B is its bending rigidity, U is the velocity of the flow, ρ_f is the fluid density, and ν is its viscosity. Most studies have also reported bistability and hysteresis regions, in which both stretched and flapping states can coexist within the same parameter range (Zhang et al., 2000; Eloy et al., 2007, 2008; Argentina & Mahadevan, 2005). Understanding the role of these parameters is therefore of primary importance. Reduced-order inviscid models, such as the vortex-sheet formulation of Shelley et al. (2005), describe the flag dynamics in terms of the mass ratio and bending rigidity, capturing the onset of instability when viscous effects are negligible. However, these models are inadequate in the low mass-ratio limit, characteristic of very light and flexible structures in water. As noted by Shelley et al. (2005), in this regime, fluid–structure coupling is strongly affected by viscous effects, which introduce additional stabilizing contributions not accounted for in inviscid formulations. This limitation was addressed by Connell & Yue (2007), who incorporated viscous effects through the Reynolds number and, via linear stability analysis, derived a criterion for the onset of flapping in viscous flows, which, for cases where the mass ratio is small compared to the added mass, reduces to:

$$S_{crit} = 1.3Re^{-0.5} + K_b k^2 \tag{2}$$

where k is the wavenumber of the perturbation. In the same work, the transition to chaotic flapping is observed at about:

$$S_{chaos} = 2.5S_{crit} \tag{3}$$

In this framework, the critical condition for instability depends on the combined effect of mass ratio, Reynolds number, and bending rigidity, highlighting the dominant role of viscous stresses in stabilizing low-inertia structures. In fact, when dealing with water flows and very flexible flags, the bending rigidity contribution might be orders of magnitude lower than the viscous one (Shelley et al., 2005), and can therefore be neglected, leaving flag flapping a function of only S and Re. However, to obtain flag flapping in water, there are three possible ways:

- increasing the flow velocity until destabilizing inertial effects become comparable to viscous/tensional stabilization, which for very light flags may require unrealistically large velocities;
- increasing the flag inertia much more than its bending rigidity, as in Shelley et al. (2005), who attached copper strips to a Mylar sheet to significantly reduce the critical velocity;
- exploiting coherent wake forcing, such as the von Kármán vortex street generated behind a bluff body, as in Allen & Smits (2001) and Wang et al. (2021). In this case, the oscillation mechanism is no longer a classical self-excited flutter instability, but rather a wake-forced lock-in or synchronization between the flag dynamics and the wake-shedding frequency.

Therefore, even in conditions where classical self-excited flutter would not be expected, externally forced oscillations may still arise through synchronization with coherent flow structures. In this context, Allen & Smits (2001) describe the simplified transverse motion of a flexible structure as a mechanical system of mass m subjected to an external forcing field:

$$m\ddot{y}(t,x) + H(\dot{y}, y, x, t) = f_1 + f_2 \tag{4}$$

where H represents the internal restoring forces associated with the structural stiffness and damping properties. The forcing term is decomposed into two contributions: f_1, representing the self-induced forcing generated by the unsteady wake produced by the structure itself (movement-induced excitation), and f_2, representing an externally induced forcing field generated remotely from the structure (extraneously induced excitation).

Similarly to Allen & Smits (2001) and Wang et al. (2021), the present work aims to exploit an external forcing field to induce the flapping motion. However, instead of the coherent von Kármán vortex street generated in the wake of a bluff body, the forcing mechanism considered here arises from the meandering dynamics of a turbulent free jet. Following the work of Miozzi & Romano (2020), the meandering motion is interpreted as the result of local transverse instabilities developing within the jet shear layers, coupled with alternating rotational structures, and amplified by their interaction with streamwise perturbations. The resulting dynamics generate a self-sustaining global oscillatory motion of the jet, which acts as an external forcing field on the flag, and may lead to synchronization phenomena in conditions where self-excited flutter would not otherwise occur.

2. Setup

The flapping of a flexible flag in a meandering water jet is here investigated by placing a Mylar sheet of dimensions $L = 0.15$ m, $h = 23 * 10^{-6}$ m and $b = 0.015$ m in front of a free-surface plane jet issuing from a slot of width $w = 0.022$ m (figures 1 and 2). The flag is clamped at its leading

edge using a fishing line of diameter $r = 20 * 10^{-6}$, to minimize disturbances introduced into the downstream flow, and is free at its trailing edge. The flag is positioned along the jet centreline, aligned with the streamwise direction, with its leading edge located at a downstream distance of $6w$ from the nozzle exit. This position was selected both to avoid the jet potential core region, which in the present setup extends approximately up to $4w$ downstream of the inlet (Sollevanti et al., 2025), and to ensure that the large-scale meandering dynamics of the jet are already well developed (Miozzi & Romano, 2020).

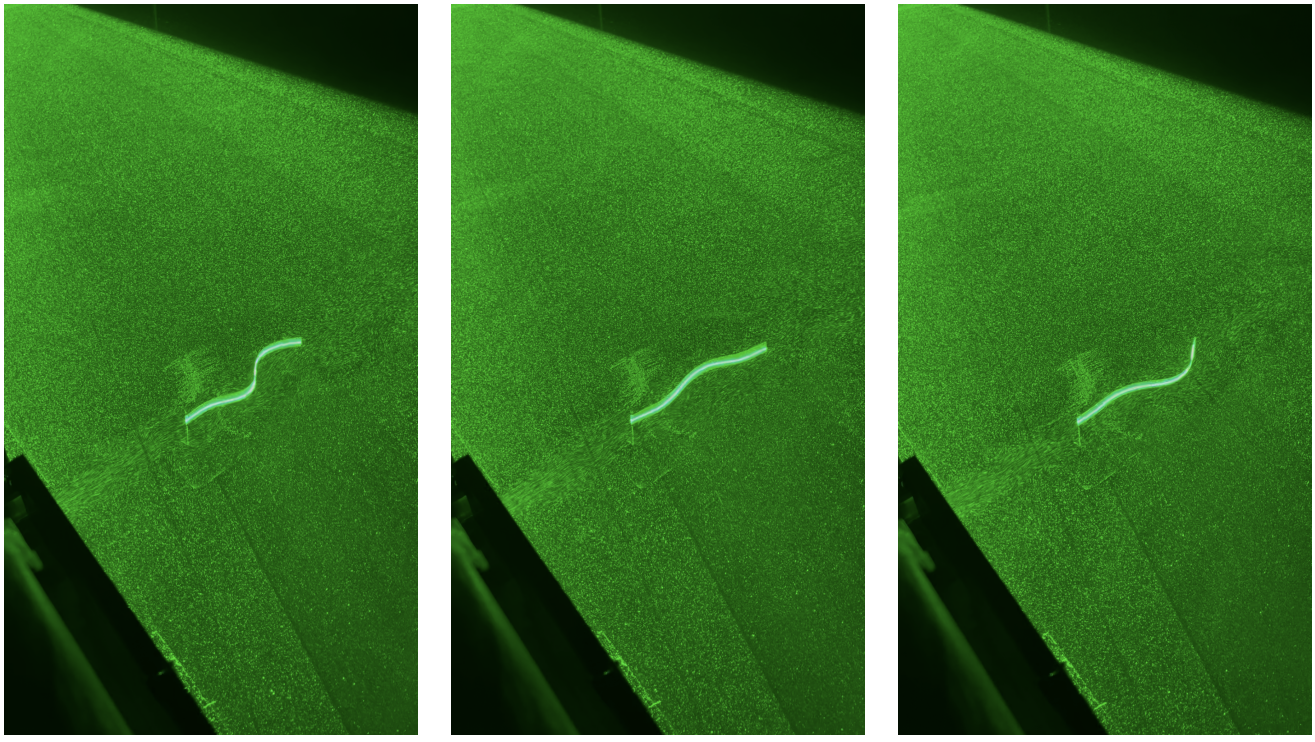


Figure 1. Snapshots of the flag's oscillations during the experiments.

Experiments are performed in a shallow free-surface water basin with an aluminum plate base (2 m × 2 m) and transparent lateral walls for optical access. A free-surface channel (approximately 1 m in length) is connected to the center of the basin to simulate a plane jet. The water jet, driven by a pump, enters the basin after passing through a reservoir (calm chamber) to dampen instabilities. Honeycombs and a convergent section are used to smooth large-scale vortical structures, while a set of trimmers induces the transition to turbulence in the inlet channel, resulting in a rectangular free-surface turbulent jet. A sharp-crested weir with V-shaped notches is installed at the opposite edge of the inlet channel to enable continuous flow discharge from the basin into the recirculating circuit. The adjustable height of the weir allows precise control of the free-surface level and flow rate (Q) within the basin. For these experiments, the flow level is maintained at $b = 0.07$ m, and the lower edge of the flag is positioned 0.03 m above the bottom plate to avoid both free-surface and bottom-wall effects. Discharged water is collected in a vessel and reintroduced into the hydraulic circuit. The water flow from the pump is regulated by an electromagnetic flowmeter located just

upstream of the channel. Flow rate fluctuations are approximately $0.1\,\mathrm{l/min}$, corresponding to less than 1% error under the experimental conditions investigated (figure 2).

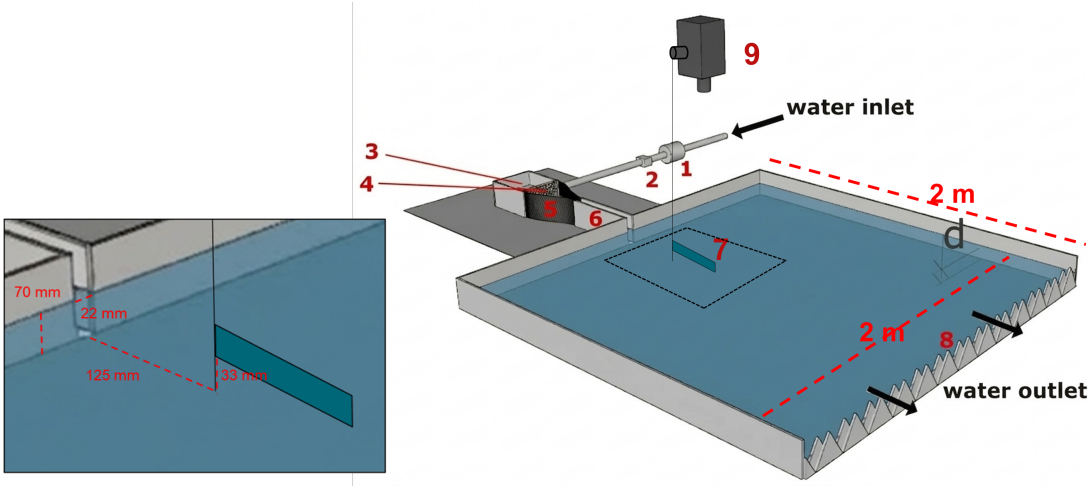


Figure 2. Sketch of the experimental setup: 1) Pump 2) Flowmeter 3) Calm chamber 4) Honeycomb 5) Convergent section 6) Inlet channel 7) Flag 8) weir 9) High-speed camera 10) Laser.

Flow images are acquired using a high-speed video camera (Fastcam NOVA S09) at frame rates ranging from 60 to 250 Hz, depending on the jet velocity for each test. The camera, with a resolution of 1 megapixel, is positioned approximately 1 m above the water's free surface. The field of view is approximately 0.22×0.22 m, yielding a pixel size of 0.21 mm in the axial direction. The reference system identifies the coordinate x to the axial direction and the coordinate y to the transverse direction (in the following, capital X and Y refer to the streamwise and transverse coordinates scaled with the inlet slot width w). Camera calibration, performed with the Camera Calibration Toolbox in MATLAB using a chessboard target, minimizes distortions from perspective and optical effects, keeping the overall reprojection error within 0.4 pixels. A shutter time of $1/7000$ s prevents motion blur under constant illumination. The characteristic turnover time of large-scale structures is approximately $\tau = 0.28$ s ($\tau \approx w/U_0 \approx 2.8 \times 10^{-1}$ s), which exceeds the acquisition time $AT = 1/60\,\mathrm{s} = 1.6 \times 10^{-2}$ s, ensuring a reliable description of large-scale structures. Spatial resolution is also good, considering that large-scale structures have sizes on the order of w, much larger than the pixel size. Illumination is provided by a 10-Watt laser placed 4.15 cm above the bottom wall, with the laser sheet intersecting the flag at mid-height. For each flow condition, 18,000 images (approximately 70 s) are recorded. The flow was seeded with neutrally buoyant hollow glass spheres with diameters between $5\mu m$ and $25\mu m$ and density $\rho_0 = 1.05 * 10^3\ kg/m^3$, resulting in a Stokes number of the order of 10^{-4}, thus allowing accurate flow tracking. The free-jet configuration has been extensively studied in previous works using the same setup (Sollevanti et al., 2025; Miozzi & Romano, 2020) and is briefly summarized in the next section, along with a few dedicated experiments.

The coupled analysis of flag motion and flow field is then carried out in two steps:

- flag identification and tracking;
- flow field analysis through PIV.

2.1. Flag identification and tracking

The flag position is identified in each frame using a dedicated MATLAB algorithm that reconstructs the flag centreline by detecting a point in each image column. The reconstructed contour is then interpolated using a cubic spline and checked for consistency with the actual flag length; errors were found to be always below 0.2 mm (≈ 1 pixel). At this stage, a number of Lagrangian markers are reconstructed along the flag by identifying, in each frame, the points located at fixed curvilinear distances from the leading edge. Their temporal trajectories are then extracted to obtain the streamwise and transverse displacement components, from which oscillation amplitudes and frequencies are computed (for more details about flag tracking and markers trajectories computation see the supplementary material at:
https://drive.google.com/drive/folders/1B9iXtziUx3KTpgD8FoLRdD5PbQt44VHn?usp=sharing).
Finally, to exclude the flag contribution from the subsequent PIV analysis, the same image-recognition algorithm is used to generate a frame-dependent polygonal mask surrounding the flag (figure 4).

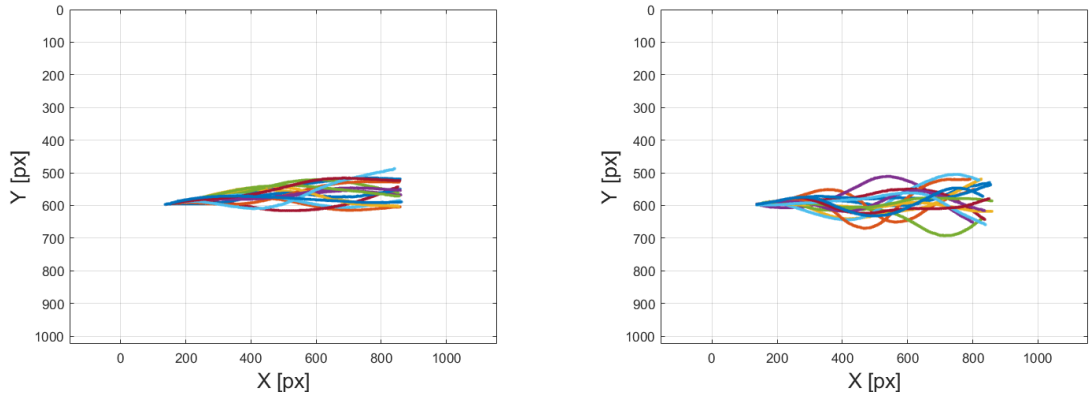


Figure 3. Identified flag position at different times for the test with $Q = 7$ l/min (left) and $Q = 21$ l/min (right).

2.2. PIV measurements

For each test, the polygonal mask identifying the flag region is applied to the images. The recorded frames are then pre-processed through background subtraction and analyzed using cross-correlation algorithms implemented in the open-source MATLAB package PIVlab (Thielicke & Stamhuis, 2014). The analysis adopts a multi-pass interrogation scheme with interrogation window sizes of $64 * 64$ pixels (first pass), $32 * 32$ pixels (second pass), and $16 * 16$ pixels (third pass), with 50%

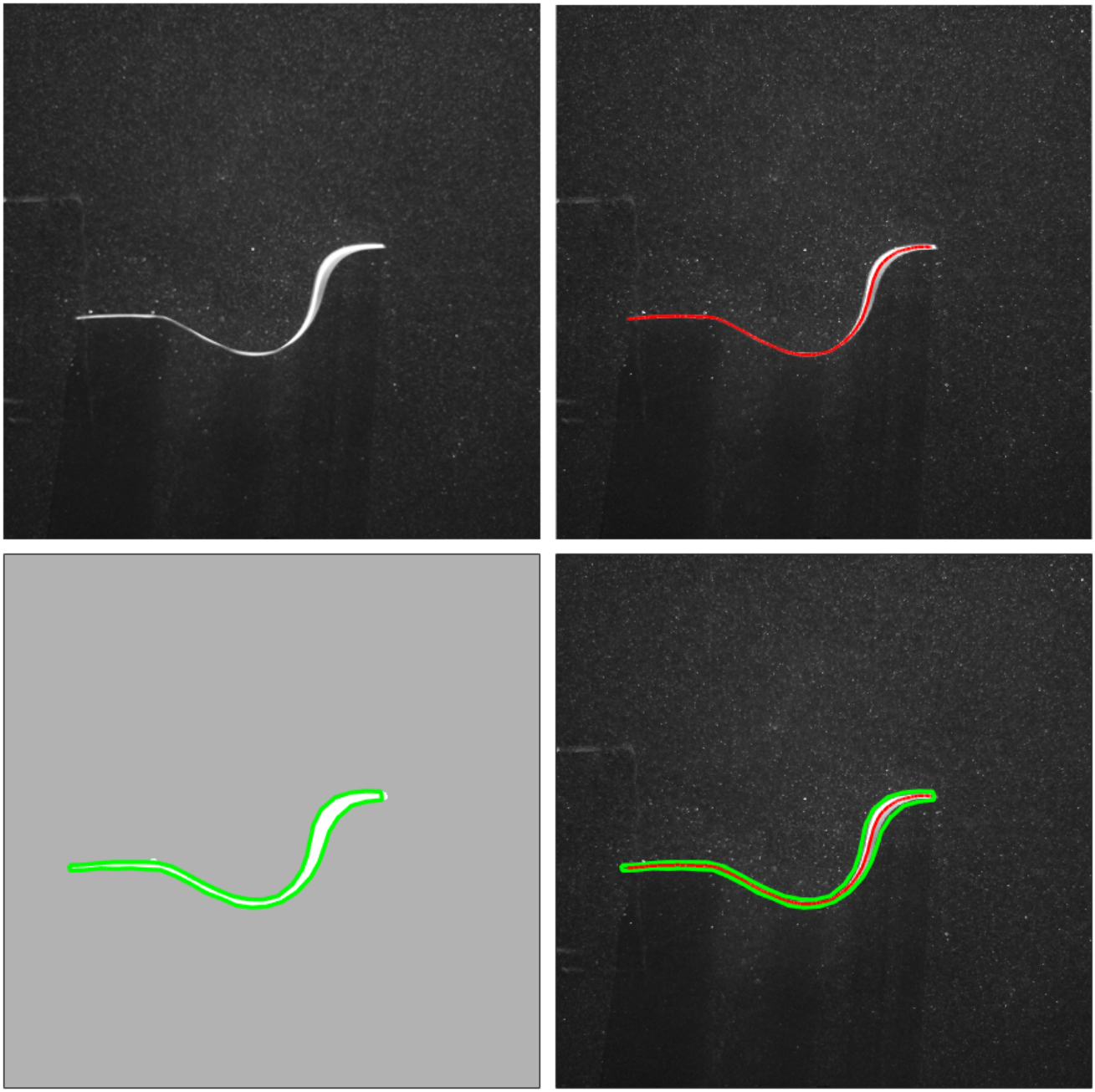


Figure 4. Flag identification and masking procedure: original frame (top-left), calculated flag contour overlaid with the original image (top-right), calculated flag-mask (bottom-left), flag contour and flag mask overlapped to the original image (bottom-right).

overlap between adjacent windows. PIV uncertainty is assessed by computing the ratio of spurious vectors to the total number of calculated vectors (Moscato & Romano, 2023). Spurious vectors are identified during the validation process through the combined application of a local median filter ($3 * 3$ window, threshold equal to 2) and a standard deviation filter (threshold equal to 3). Detected spurious vectors are removed and replaced through interpolation. In all cases, interpolated vectors remain below 2% of the total vector count.

Once the flag position and the flow field have been calculated separately, the two are combined to obtain a coupled description of the fluid–structure dynamics (see figure 5). However, due to the limited spatial resolution and the finite size of the polygonal mask surrounding the flag, reliable measurements of velocity gradients in the immediate vicinity of the flag were not possible. Nevertheless, since the present work focuses on the global coupling between the large-scale jet dynamics and the flag motion, rather than on the detailed estimation of local hydrodynamic stresses on the flag surface, this limitation does not affect the main objectives of the analysis.

In the next sections, we present the results of the analysis carried out over a range of Reynolds numbers by varying the jet velocity, as summarized in Table 1. The evolution of both the jet meandering dynamics and the flag oscillatory motion is then discussed to identify the mechanisms underlying the synchronization between jet fluctuations and flag motion.

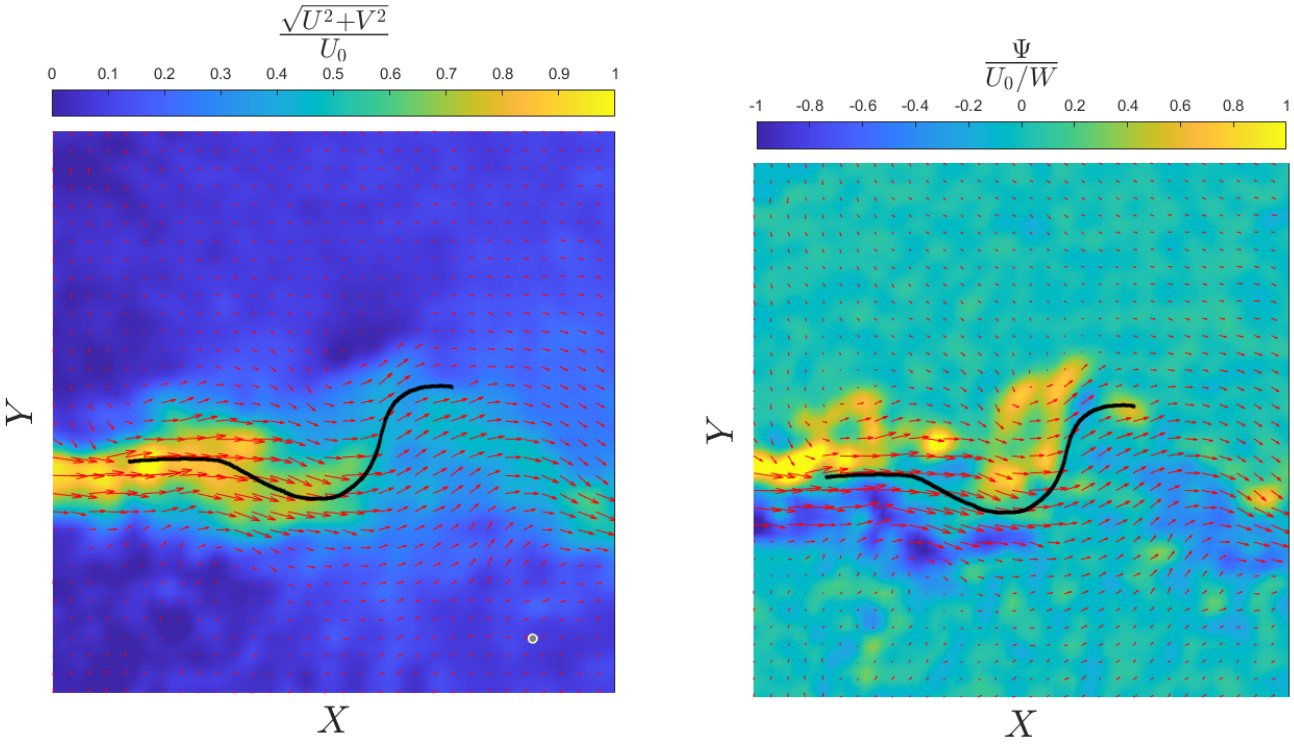


Figure 5. Instantaneous velocity magnitude (left) and vorticity contours (right), overlaid with the calculated velocity vectors (red) and the identified flag position (black).

Test ID	Q [l/min]	U_0 [m/s]	Re_L	Re_w	Fr
Test 1	7	0.077	12000	1800	0.09
Test 2*	9	0.099	15000	2200	0.12
Test 3	12	0.132	20000	3000	0.16
Test 4*	15	0.165	25000	3700	0.20
Test 5	18	0.195	30000	4400	0.24
Test 6*	21	0.224	34000	5100	0.27

Table 1. Details of the experimental tests considered in this work. Tests IDs marked with the "*" have also been carried out in the simple free-jet configuration. Note that Re_w is based on w as the reference length instead of L.

3. Results and discussion

3.1. Free jet

From the PIV analysis of the free jet, we report some well-known properties of this jet configuration that agree very well with previous work from our laboratory in the same setup and under similar experimental conditions (Sollevanti et al., 2025; Miozzi & Romano, 2020). These preliminary results confirm that, in all conditions considered, the jet behaves somewhat halfway between a plane jet and a fully three-dimensional one. In fact, in the mean-field limit, the axis velocity decay is linear, as in three-dimensional jets, while transverse spreading, associated with ambient fluid entrainment, is closer to that of a plane jet (Sollevanti et al., 2025), especially at low flow rates, as shown in figure 6. Figure 8 also shows that the measurement region is well outside the jet's core and within the self-similarity region, as the scaled transverse velocity profiles collapse onto one another, with no constant-velocity region characteristic of the jet core observed. The turbulence intensity is similar across all tested flow rates, with peaks of about $20 - 22\%$ occurring in the shear layers (figure 7).

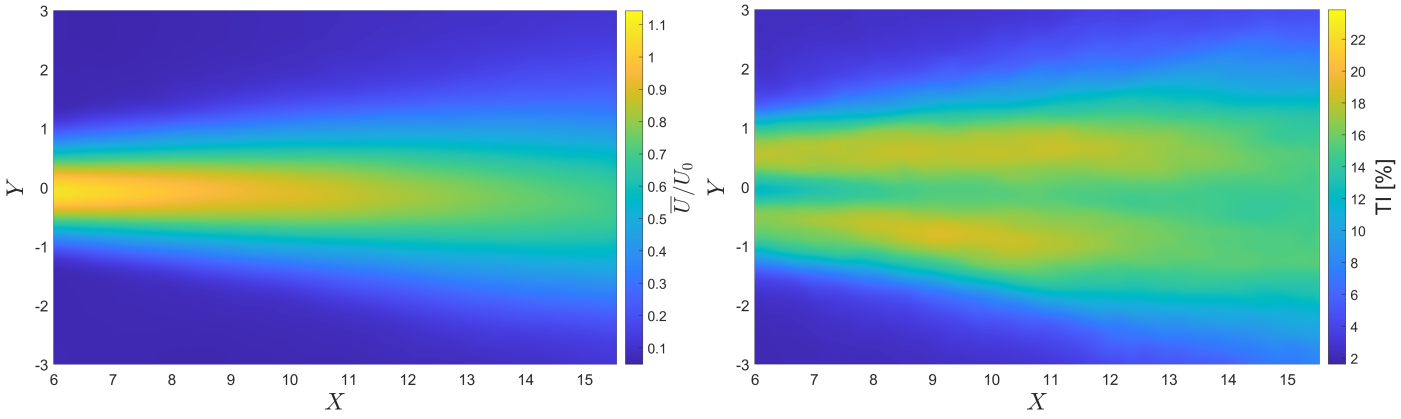


Figure 7. Mean velocity magnitude (left) and turbulence intensity (right) maps for the 21 l/min free-jet case.

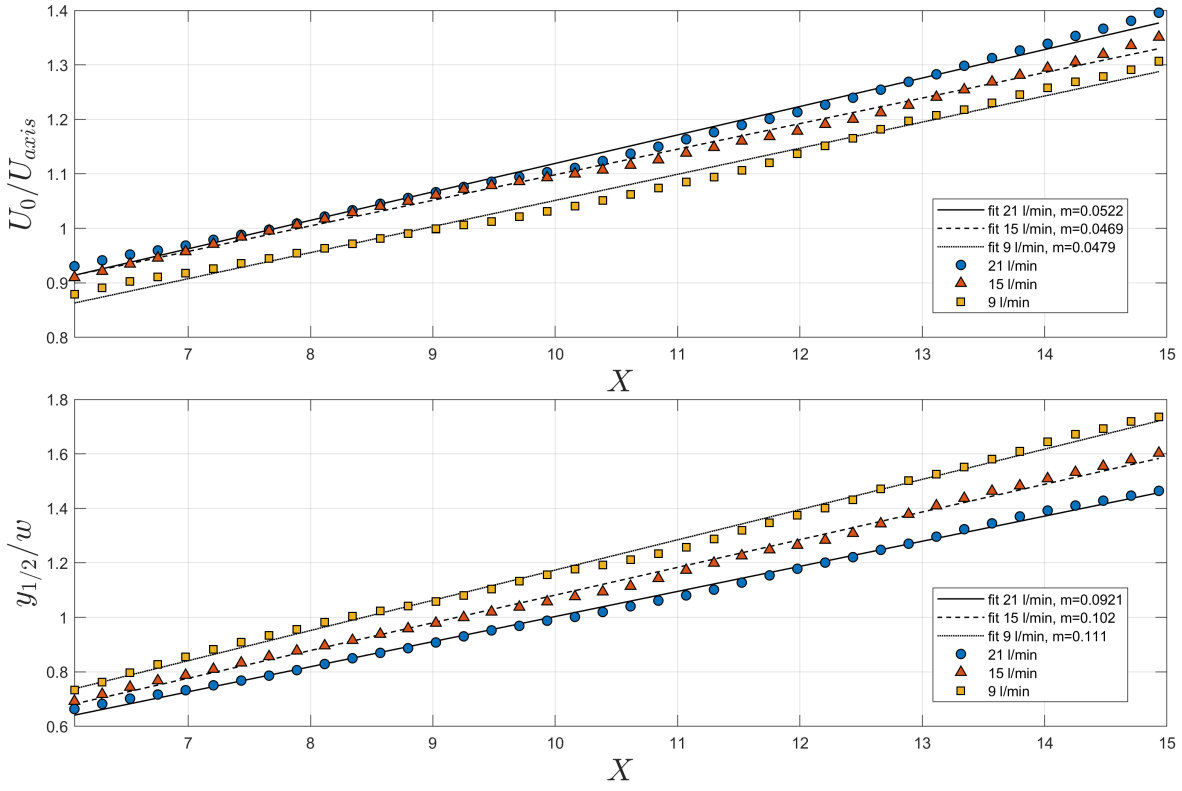


Figure 6. Streamwise evolution of the inverse centreline velocity decay, U_0/U_{axis}, and lateral half-width spreading of the free jet.

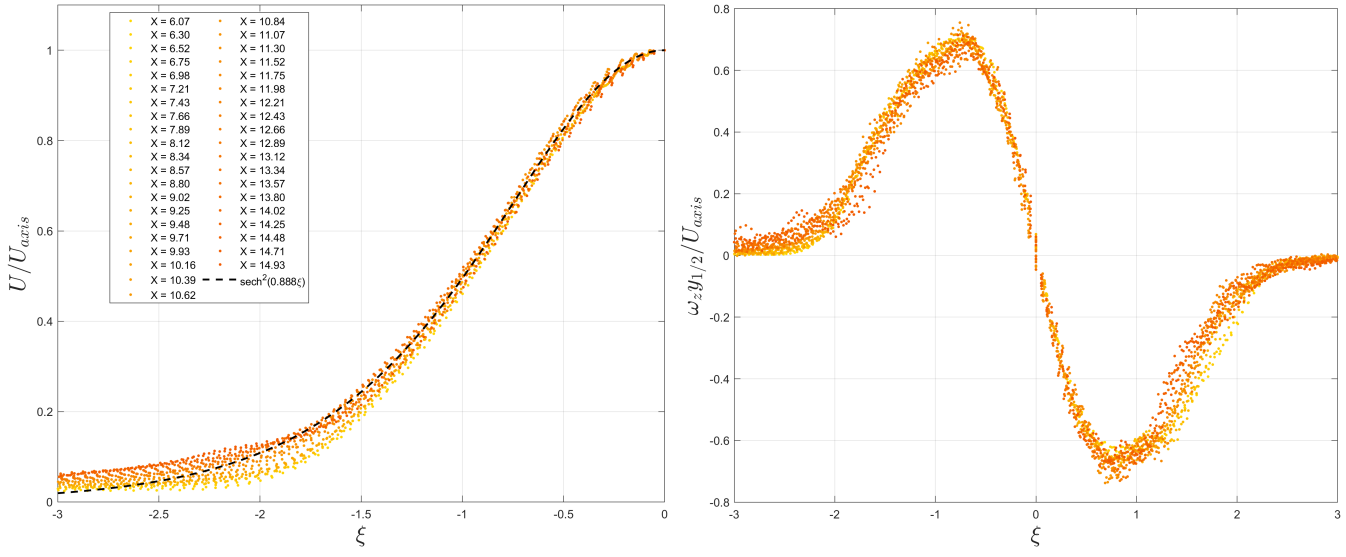


Figure 8. Collapsed transverse profiles of mean streamwise velocity (left) and mean vorticity (right) for the 21 l/min free-jet case.

A classical meandering analysis, based on the spectral approach of Miozzi & Romano (2020), was then carried out on the transverse velocity component measured along the centreline and is presented in figure 9. The results show that, away from the near field, the Strouhal number associated with the meandering motion tends to plateau along the streamwise direction, within the range $0.08 < St < 0.1$ (figure 9-top). The characteristic frequencies for each case are instead reported in figure 9-center and depend on the jet flow rate, but remain rather constant along the X-direction, with well-defined peaks at about 1, 0.55, and 0.4 Hz for the tests corresponding to Reynolds numbers (Re_L) of 34000 ($Q = 21$ l/min), 25000 ($Q = 15$ l/min), and 15000 ($Q = 9$ l/min), respectively. Meandering amplitudes were quantified as the root-mean-square temporal displacement of the instantaneous centreline from its mean position, normalized by the nozzle width (w), and plotted as a function of X (figure 9-bottom). The normalized centreline displacement RMS increases linearly with downstream distance at all flow rates, indicating a progressive increase in the geometric meandering amplitude as the jet develops downstream.

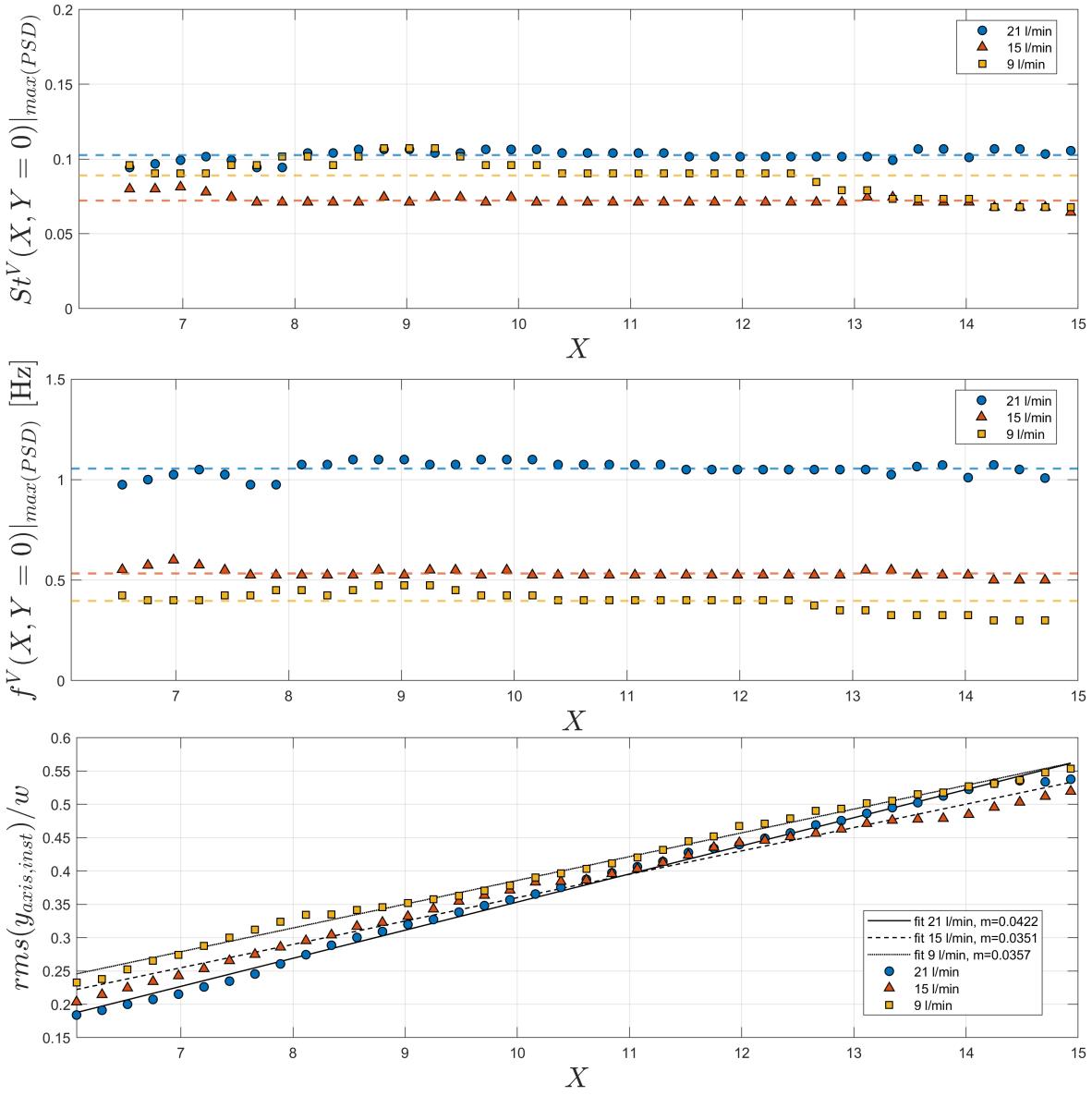


Figure 9. Streamwise evolution of the dominant Strouhal number (top), dominant transverse-velocity frequency (center), and RMS of the instantaneous centreline displacement for the free jet (bottom).

3.2. Flag analysis

A preliminary visual inspection of the videos, obtained by superimposing the instantaneous flow-field contours, either velocity magnitude or vorticity, onto the flag position (of which figure 5 shows one representative frame), suggests that the flag dynamics is strongly affected by the large-scale transverse perturbations associated with jet meandering. These perturbations appear to force the flag response, promoting synchronization with the characteristic meandering frequencies of the free jet. To analyze this behavior, we first rely on the motion of Lagrangian markers distributed along the flag, as described in the previous section. The marker time histories are reported for both

the streamwise and transverse displacements at different flow rates. The transverse displacement displays a coherent, although irregular, oscillatory motion (figure 10), whereas the streamwise component is more intermittent and impulsive, with snapping-like events like those reported by Connell & Yue (2007) in the strongly nonlinear flapping regime (figure 11). In both directions, the oscillation amplitude increases from the leading edge towards the trailing edge, but with different spatial trends: the transverse amplitude grows slightly sub-linearly, while the streamwise component shows an almost quadratic increase (figure 12).

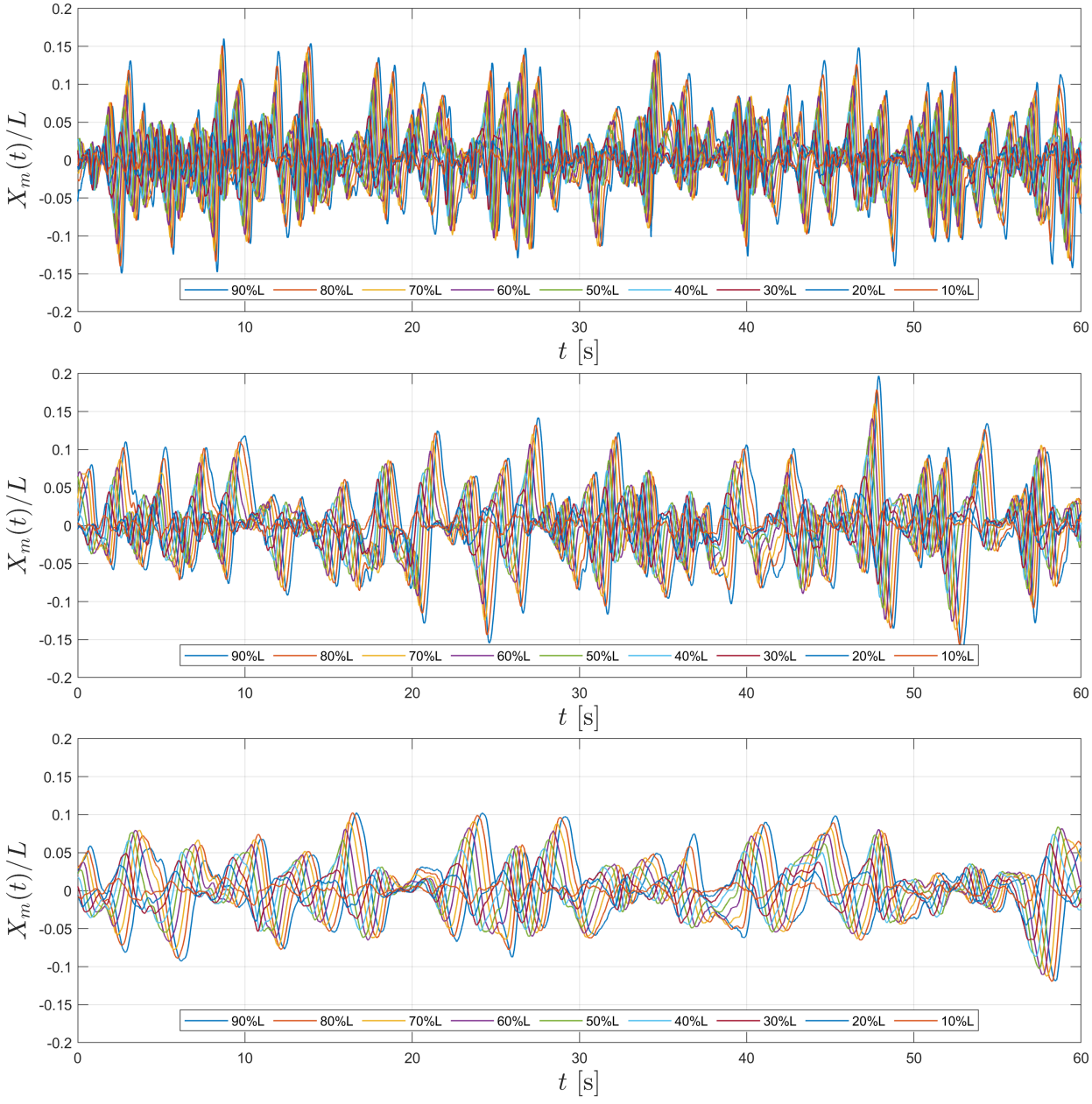


Figure 10. Time-series of the transverse displacement of 9 markers distributed along the flag length at different flow rates: 21 l/min (top) – 15 l/min (middle) – 9 l/min (bottom). The legend indicates the marker's distance from the leading edge of the flag as a percentage of the flag's total length.

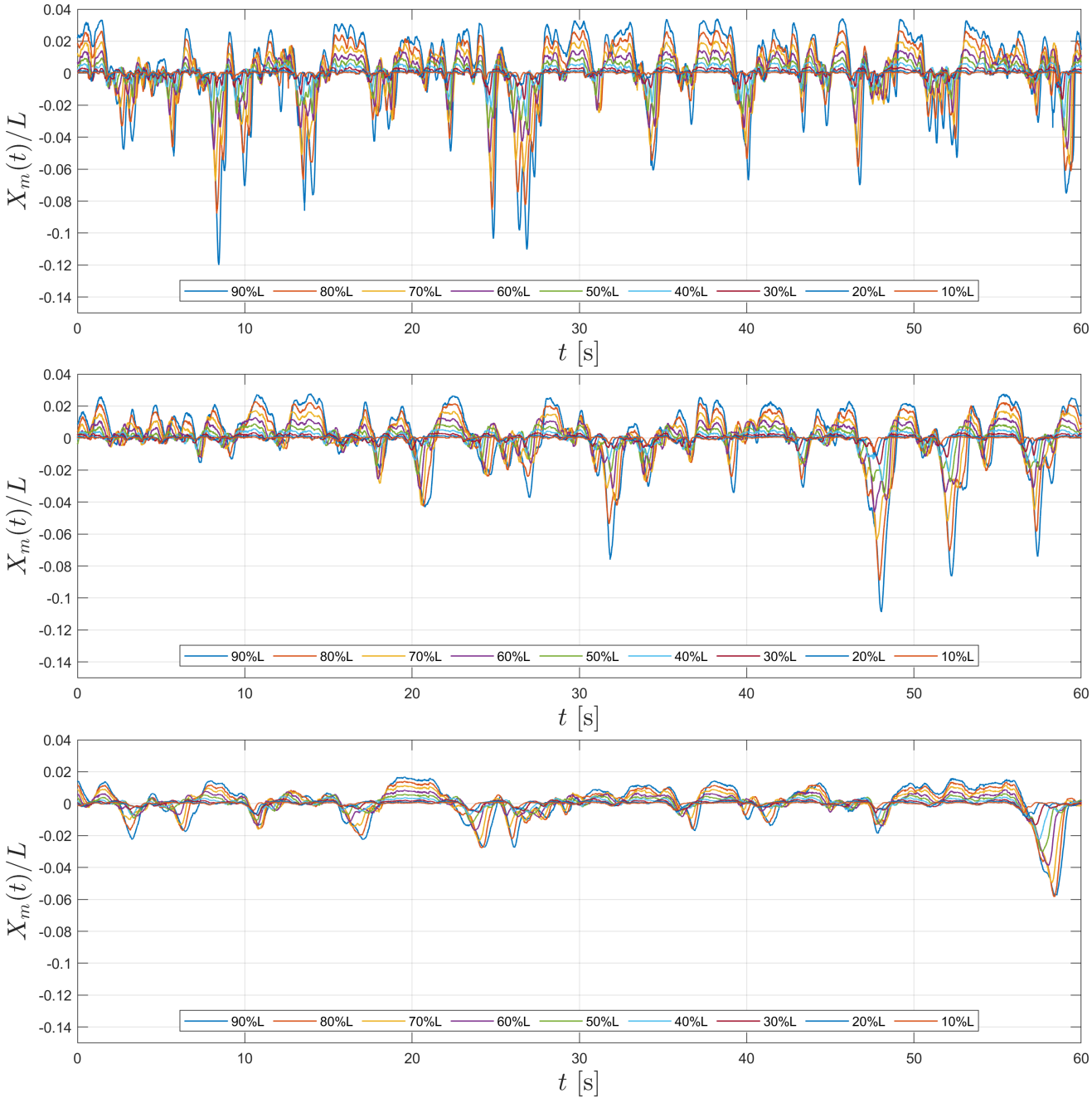


Figure 11. Time-series of the streamwise displacement of 9 markers distributed along the flag length at different flow rates: 21 l/min (top) – 15 l/min (middle) – 9 l/min (bottom). The legend indicates the marker's distance from the leading edge of the flag as a percentage of the flag's total length.

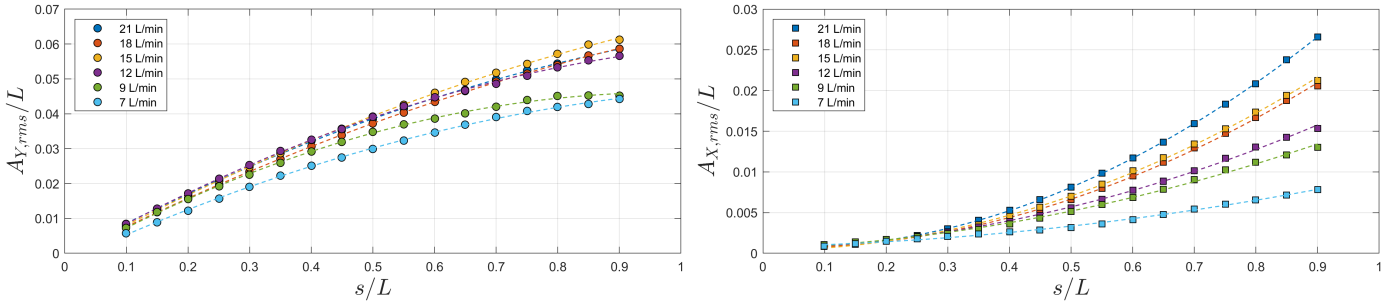


Figure 12. RMS amplitude of the normalized marker displacements along the flag: transverse component A_{Y-rms}/L (left) and streamwise component A_{X-rms}/L (right), for the different flow rates. Dashed lines denote polynomial fits used to highlight the different spatial growth trends of the two components.

To investigate the spatio-temporal organization of the flag deformation, the transverse displacement was re-sampled at closely spaced markers distributed from 10% to 90% of the flag length, with a spacing of 5%, and represented as a space-time map of $Y_m(t)/L$ (figure 13). The resulting alternating positive and negative displacement bands exhibit a clear inclination along s/L, revealing that the deformation is not in phase over the entire flag, but is instead convected downstream as a travelling-wave-like motion. This observation further supports the hypothesis that the flag response is driven by the meandering dynamics of the jet, consistently with the convectively propagating perturbations described by Miozzi & Romano (2020).

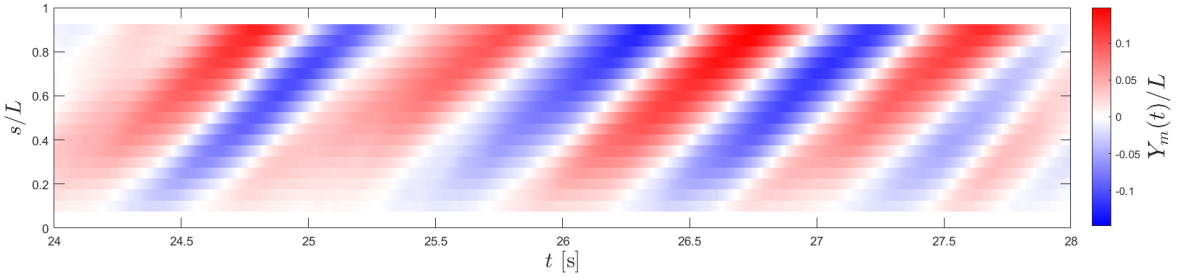


Figure 13. Space-time map of the normalized transverse flag displacement $Y_m(t)/L$ for the 21 l/min case, reconstructed from markers distributed along the flag length. The inclined alternating positive and negative displacement bands indicate a downstream phase progression of the deformation, showing that the flag motion is not synchronous along s/L but exhibits a traveling-wave-like convective character.

For the spectral characterization, however, we do not rely directly on the dominant peaks of the marker-displacement PSDs estimated through Welch's method. These peaks were found to be sensitive to the selected Hamming-window length, especially when multiple competing spectral components had comparable amplitudes. A more robust description of the dominant dynamics was therefore obtained through a POD-like decomposition based on the singular-value decomposition (SVD) of the discrete spatio-temporal fluctuating field after subtraction of the time average. This approach was applied to both the flag-deformation field and the transverse-velocity signal

measured along the jet centreline, allowing the dominant spatial structures and their associated temporal coefficients to be compared between the structural response and the forcing flow.

3.3. Proper Orthogonal Decomposition

The modal decomposition provides a compact representation of the coupled dynamics, separating the spatial organization of the deformation/velocity fields from their temporal evolution and enabling a direct comparison between the flag response and the meandering motion of the free jet. With the POD-like decomposition, both the flag transverse deformation and the jet transverse-velocity signal are represented in the form:

$$q(x,t) = \overline{q}(x) + \sum_{m=1}^{N} a_m(t)\phi_m(x) \tag{5}$$

where $\phi_m(x)$ are the spatial modes, $a_m(t)$ are the corresponding temporal coefficients describing the time evolution of each mode, q(x,t) is either $Y(x,t)$ (the transverse displacement of the flag) or $V(x,t)$ (the transverse velocity component of the free jet measured along its centreline) and $\overline{q}(x)$ is the time-averaged field considered. The results of the analysis are reported in figures 14-17 for the free jet and 18-22 for the flag deformation. In particular, for the jet ($V(x,t)$) and the flag deformation ($Y(x,t)$) respectively, figures 14 and 18 show the spatial modes along X, figures 15 and 19 report the time-series of the corresponding temporal coefficients, figures 16 and 20 the unwrapped spatial phase along the temporal coefficients ($a_1(t)$ vs $a_2(t)$) phase portrait, figures 17 and 21 show the modal energy of the first modes at each flow rate and the corresponding characteristic frequencies. Additionally, for the flag deformation only, figure 22 (bottom) compares the first spatial mode across the different flow rates, while figure 22 (top) shows the mean flag shape overlaid with the deformation associated with each of the first four spatial modes.

By comparing figures 17-left and 21-left, a first important difference emerges from the modal-energy distribution: while the flag deformation is almost entirely described by the first two modes, which contain more than 85% of the total energy, the free-jet centreline velocity exhibits a more distributed modal content, with the first two accounting for less than 30%, consistently with the turbulent nature of the jet. However, considering the first two modes, their characteristic frequencies, evaluated from the PSD of the corresponding temporal coefficient ($a_m(t)$), are found to be very close between the flag response and the transverse-velocity fluctuations of the free jet, indicating that the dominant structural dynamics occur at nearly the same time scales as the meandering motion of the jet. This contrast suggests that the flag acts as a selective structural filter: although the flow contains a broader range of spatial and temporal fluctuations, the flag response organizes itself mainly through a dominant two-mode dynamics. The convective nature of the meandering motion of the jet, and therefore of the flag response, is well represented in figures 16 and 20,

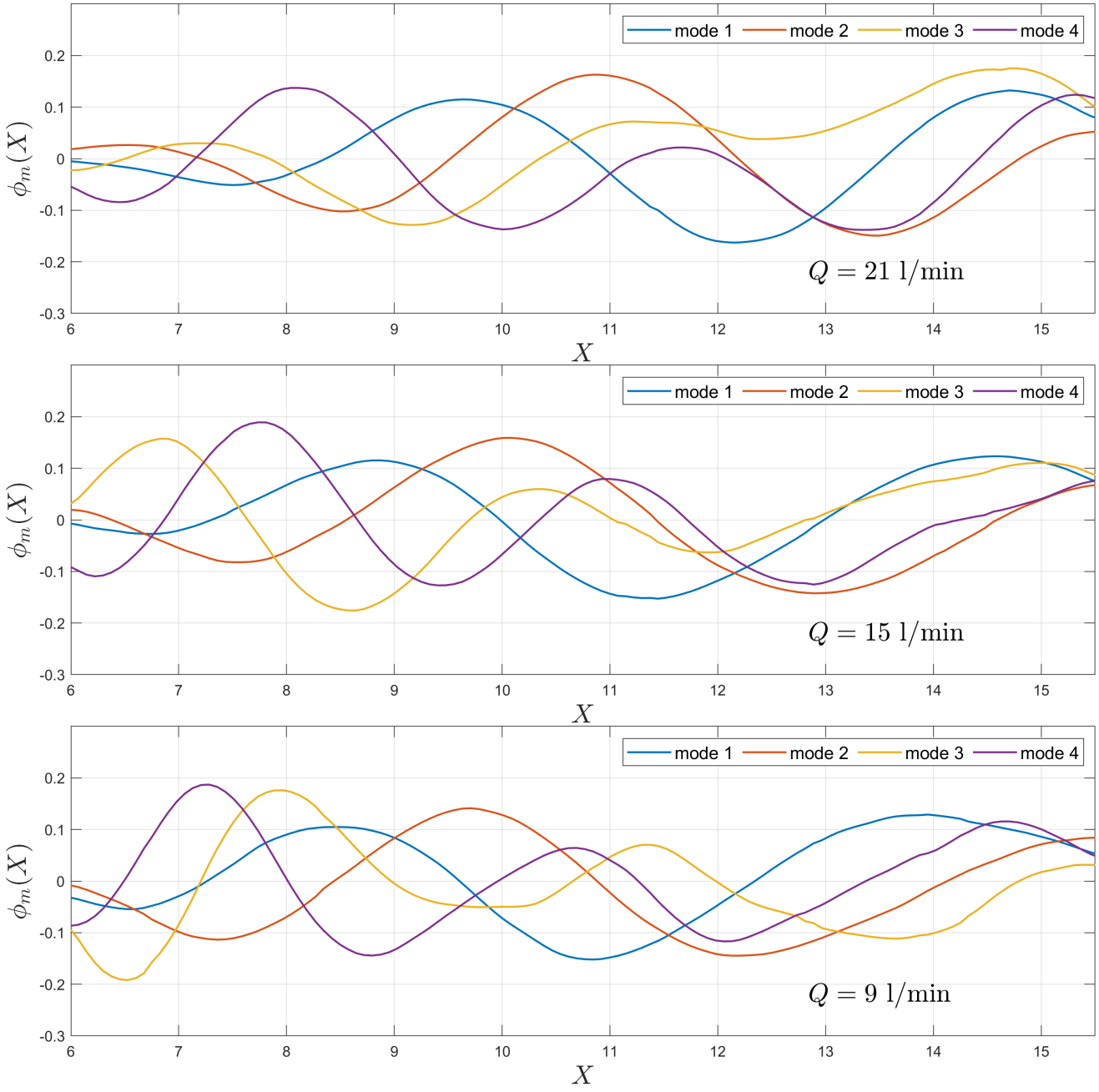


Figure 14. POD analysis of the free-jet transverse velocity measured along the jet centreline: first four spatial modes of $V(x,t)$ at $Q = 21$ l/min (top), $Q = 15$ l/min (center) and $Q = 9$ l/min (bottom).

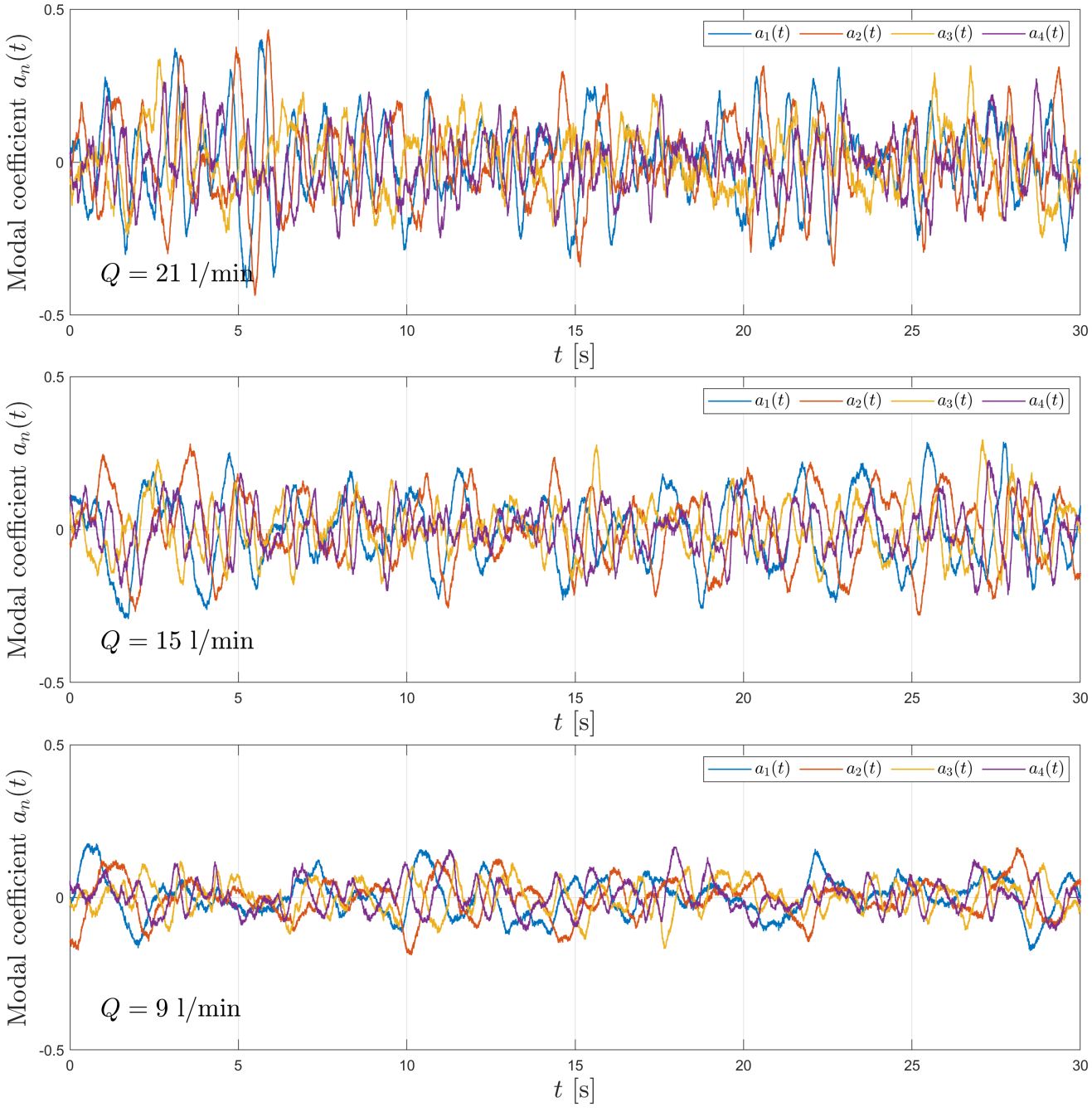


Figure 15. POD analysis of the free-jet transverse velocity measured along the jet centreline: time-series of the temporal coefficients corresponding to the first four spatial modes of $V(x,t)$ at $Q = 21$ l/min (top), $Q = 15$ l/min (center) and $Q = 9$ l/min (bottom).

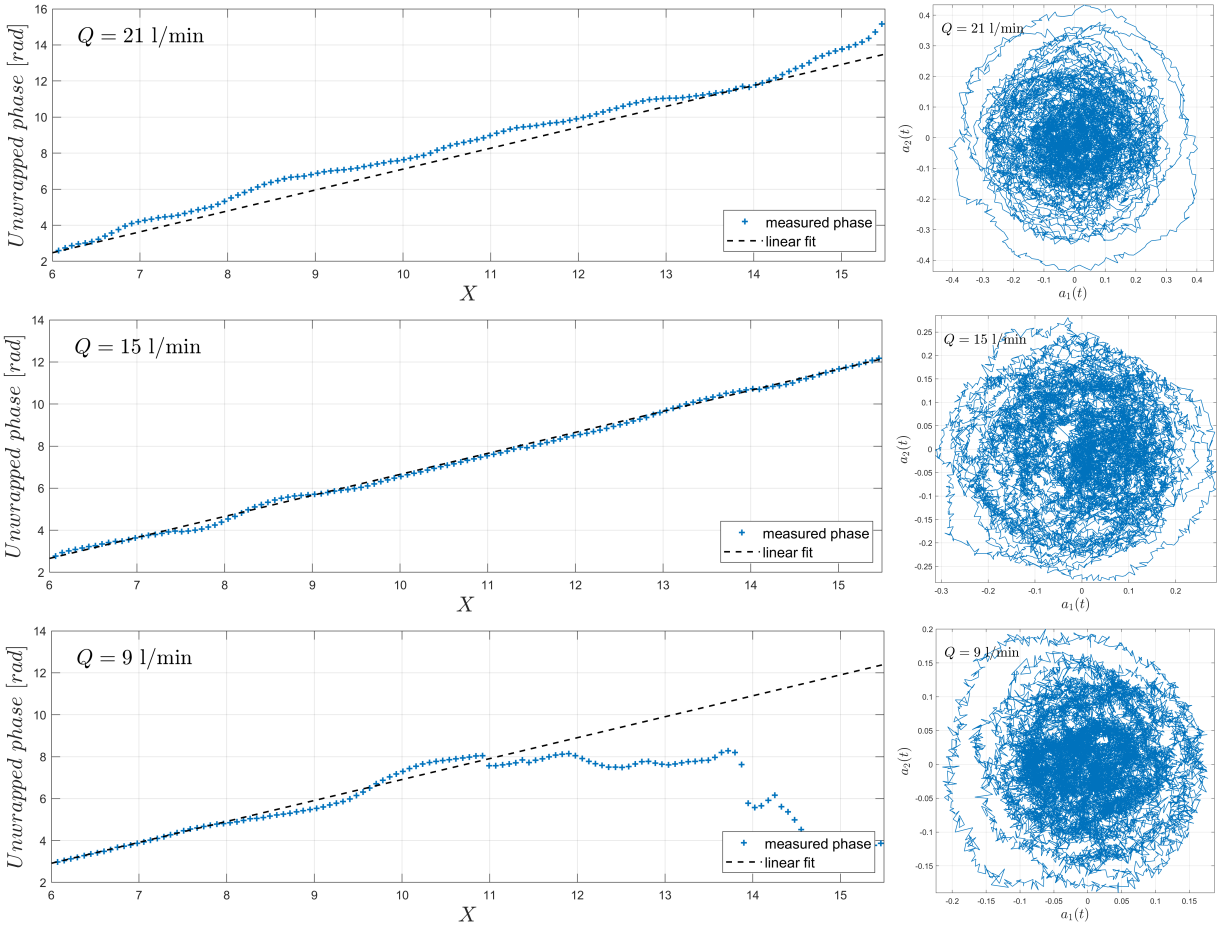


Figure 16. POD analysis of the free-jet transverse velocity measured along the jet centreline. For each flow rate, the left panel reports the unwrapped spatial phase of the dominant modal pair as a function of the streamwise coordinate, while the right panel shows the corresponding phase portrait of the first two temporal coefficients, $a_1(t)$ and $a_2(t)$.

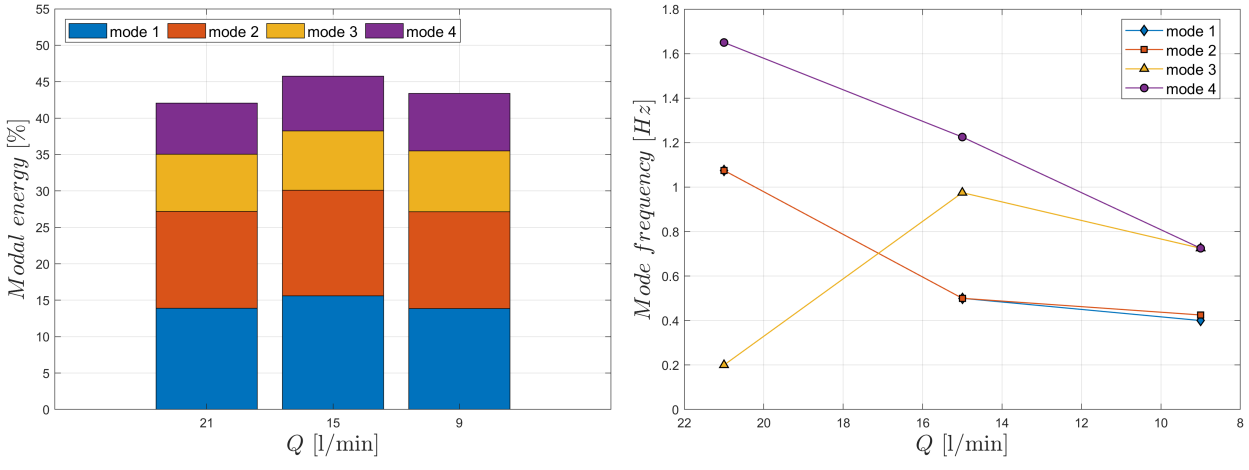


Figure 17. POD modal content of the free-jet transverse velocity measured along the jet centreline. Left: cumulative contribution of the first four modes to the total fluctuation energy at the investigated flow rates. Right: characteristic frequencies of the first four POD temporal coefficients, estimated from their PSDs.

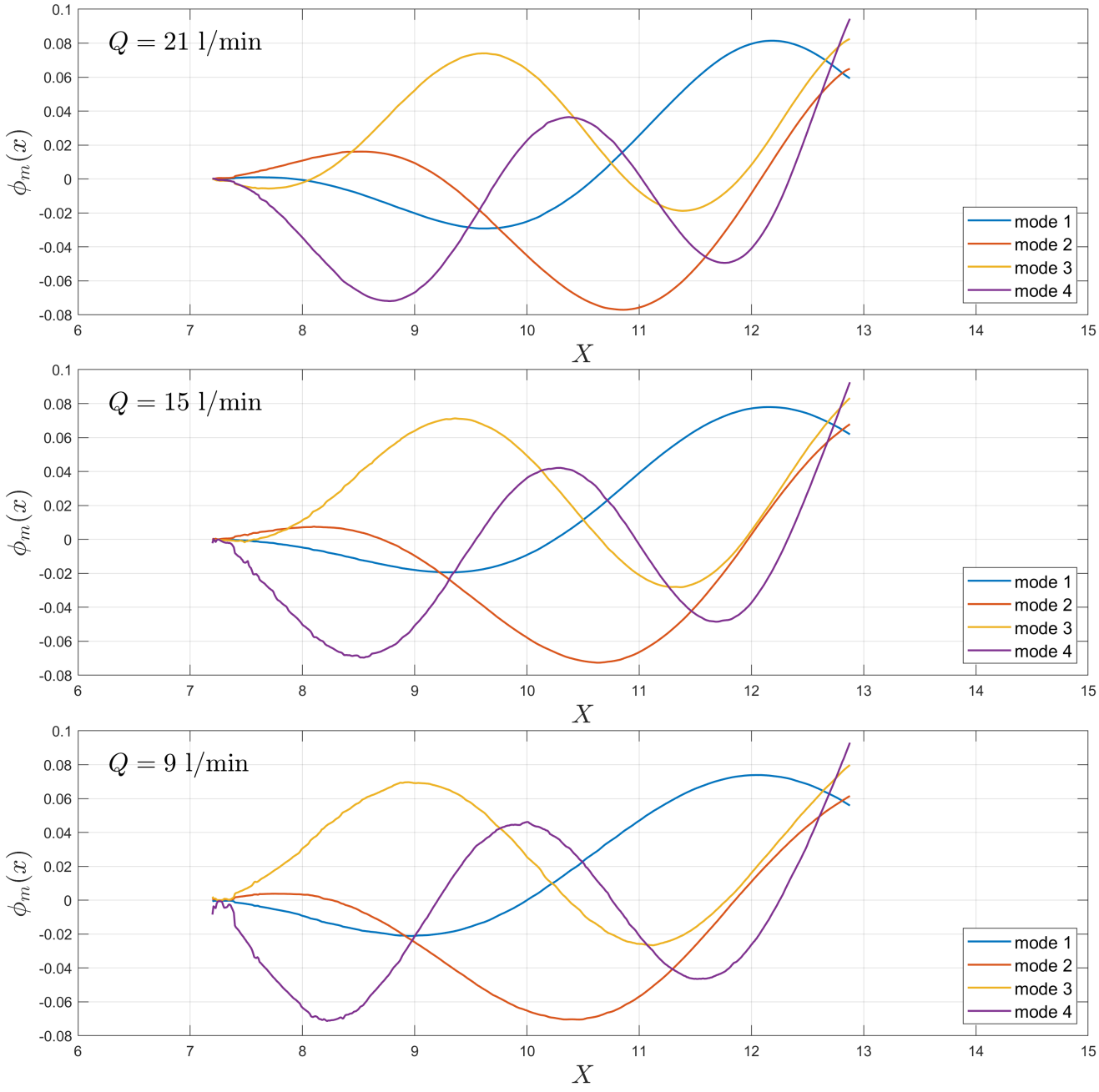


Figure 18. POD analysis of the flag deformation: first four spatial modes of $Y(x,t)$ at $Q = 21$ l/min (top), $Q = 15$ l/min (center), and $Q = 9$ l/min (bottom).

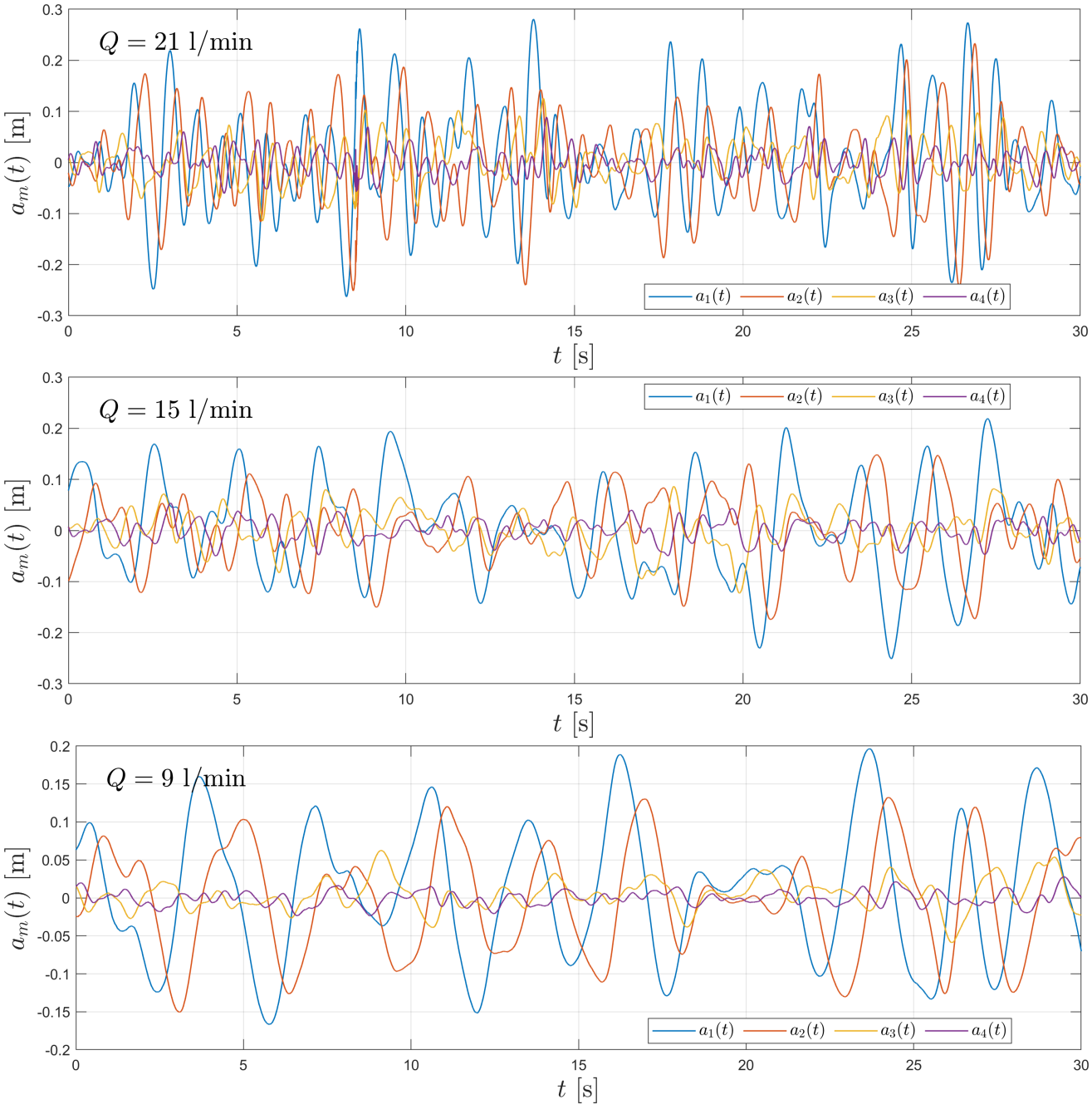


Figure 19. POD analysis of the flag deformation: time-series of the temporal coefficients corresponding to the first four spatial modes of $Y(x,t)$ at $Q = 21$ l/min (top), $Q = 15$ l/min (center), and $Q = 9$ l/min (bottom).

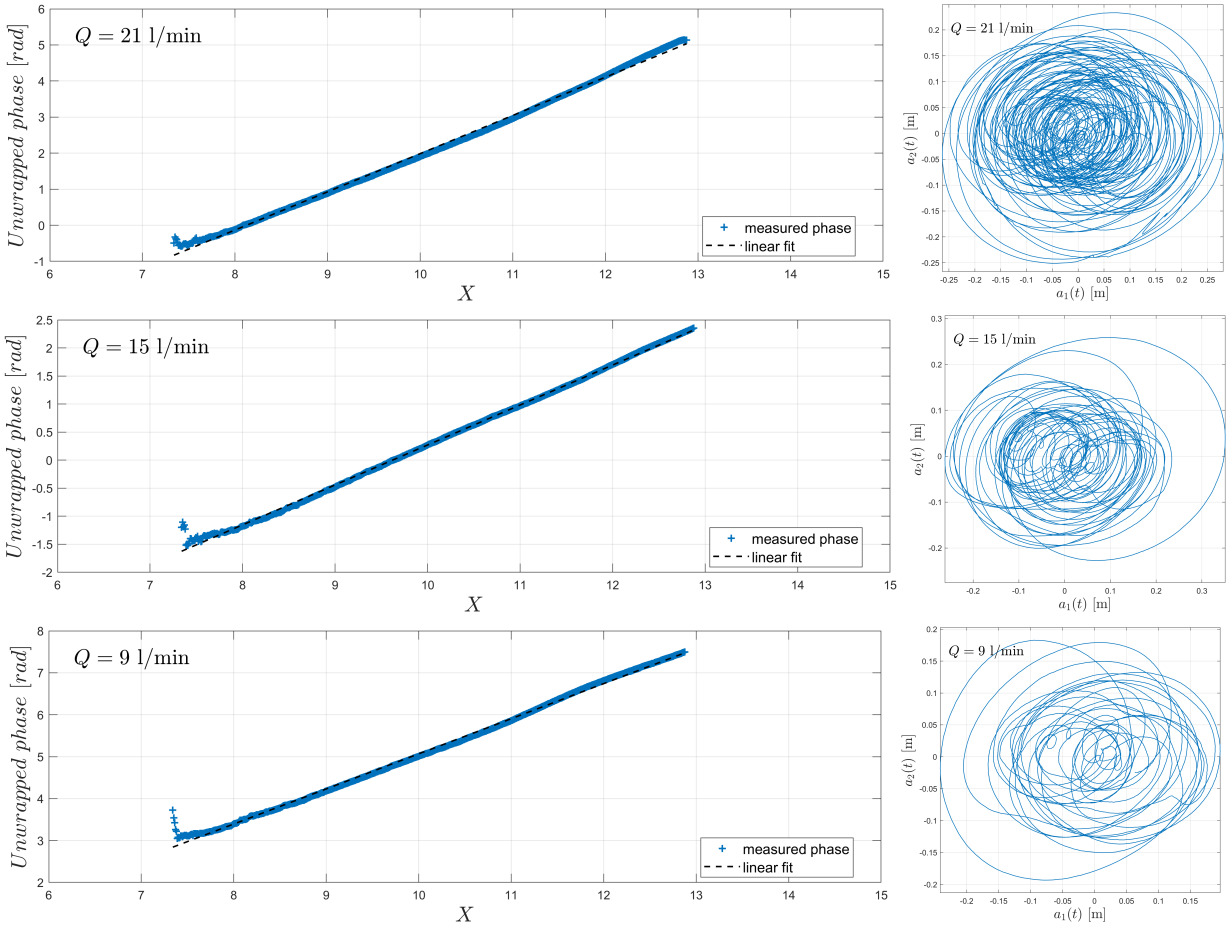


Figure 20. POD analysis of the flag deformation: for each flow rate, the left panel reports the unwrapped spatial phase of the dominant modal pair as a function of the streamwise coordinate, while the right panel shows the corresponding phase portrait of the first two temporal coefficients, $a_1(t)$ and $a_2(t)$.

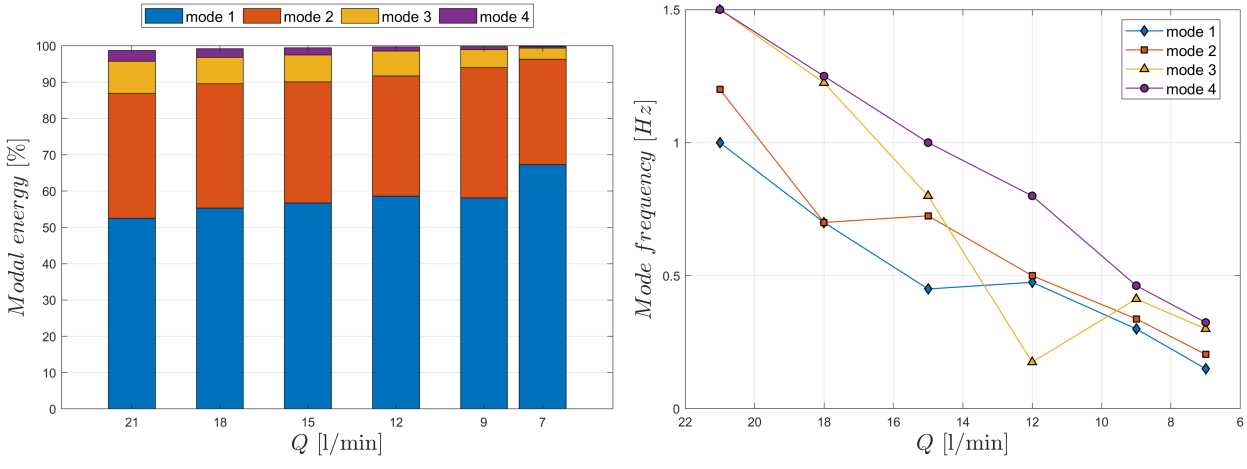


Figure 21. POD modal content of the flag deformation. Left: cumulative contribution of the first four modes to the total fluctuation energy at the investigated flow rates. Right: characteristic frequencies of the first four POD temporal coefficients, estimated from their PSDs.

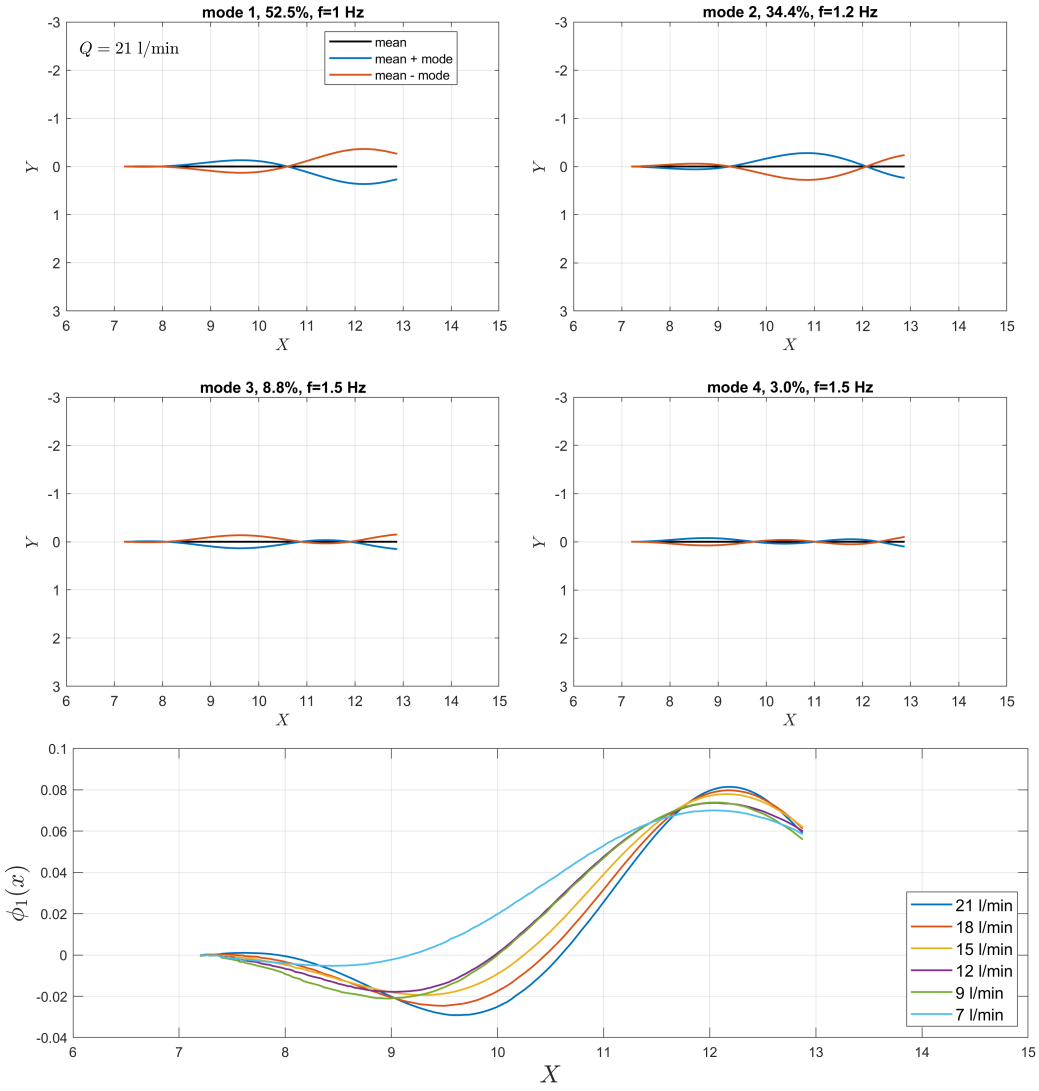


Figure 22. Flag deformation reconstructed from the POD modes. Top: mean flag shape for the 21 l/min case overlaid with the positive and negative deformation associated with the first four modes. Bottom: comparison of the first spatial POD mode of the flag deformation at the different flow rates.

where the unwrapped spatial phase and the temporal coefficients ($a_1(t)$ vs $a_2(t)$) phase portrait are shown for the jet and the flag, respectively. The near-linear increase of the unwrapped phase along (X) indicates a progressive phase delay in the streamwise direction, characteristic of convective perturbations. At the same time, the $a_1(t)$-$a_2(t)$ phase portraits show rotating, elliptical-like trajectories, indicating that the first two modes act as a coupled modal pair with an approximately quadrature phase relationship. This behavior is observed in both the free-jet velocity field and the flag deformation, confirming the convective nature of the meandering motion and supporting the interpretation of the flag motion as a traveling-wave-like response driven by the meandering dynamics of the jet.

Furthermore, by computing the slope from the linear fit of the unwrapped phase, we obtain an estimate of the spatial wavenumber of the propagating disturbance ($k = d\phi/dx$) and, consequently, of its phase velocity ($c = 2\pi f/k$, where f is the dominant frequency calculated from the PSD of $a_1(t)$) and spatial wavelength ($\lambda = 2\pi/|k|$)). The ratio of these parameters for the flag and the jet is shown in figure 23 as a function of the flow rate. These ratios remain close to unity over the investigated flow-rate range, therefore confirming that the flag does not oscillate independently but is forced by the meandering motion of the jet, which imposes its characteristic temporal and convective scales on the structural response.

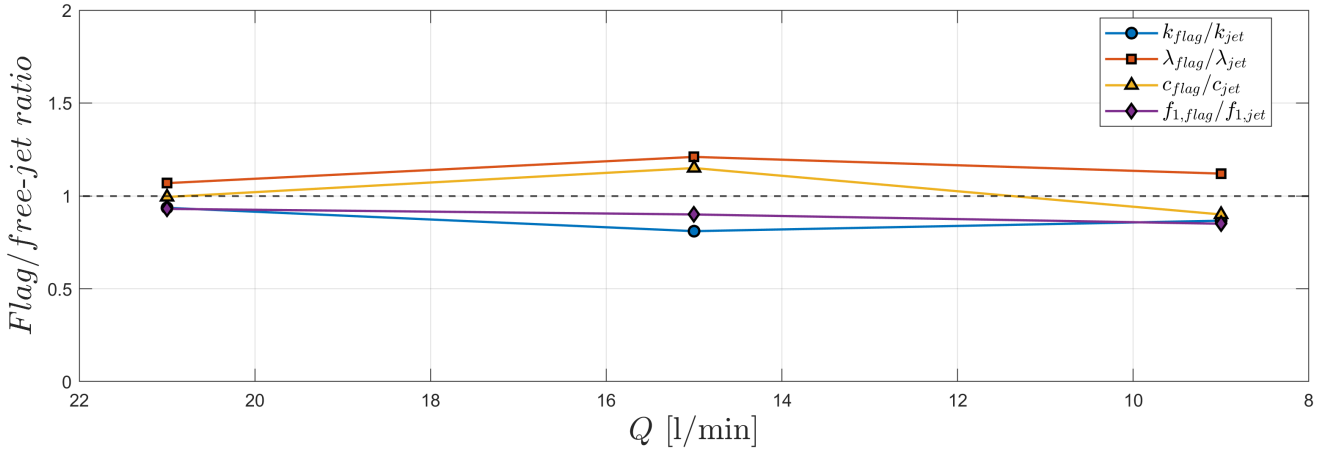


Figure 23. Comparison between the convective scales extracted from the POD analysis of the flag deformation and of the free-jet transverse velocity. The ratios of wavenumber, wavelength, phase velocity, and dominant first-mode frequency are reported as a function of the flow rate; values close to unity indicate matching temporal and convective scales between the flag response and the jet meandering.

4. Conclusions

In this work, we have studied the interaction and coupled dynamics between a turbulent water jet and a light, flexible Mylar flag. Since the classical self-sustained flag flutter is not easily induced for low-inertia flags immersed in water jets, due to the additional stabilizing contributions of viscous effects (Shelley et al., 2005), we instead explored the possibility of triggering flag oscillation and flapping through an externally imposed flow unsteadiness (Allen & Smits, 2001; Wang et al., 2021). Unlike previous approaches based on vortex shedding in the wake of bluff bodies, here the forcing mechanism is provided by the jet's intrinsic meandering instability. In fact, once sufficiently developed, the meandering motion exhibits characteristic frequencies that are relatively stable along the streamwise direction and can be tuned through the inlet flow rate (Miozzi & Romano, 2020), making it a suitable candidate for imposing organized oscillations on flexible structures. Our experiments show that, in this way, flapping is accessible, also in water, at very low velocities, and that the flag's oscillations are strongly synchronized with the meandering dynamics of the jet. The dominant frequencies extracted from the flag motion match those measured in the free jet at the corresponding flow rates, while the amplitude of the flag oscillation increases along the flag length, indicating a progressive development of the deformation from the leading edge toward the trailing edge. This interpretation is further supported by the POD analysis, which shows that the flag response is dominated by a small number of coherent modes, whereas the free-jet velocity field retains a broader modal content. Despite this difference, the dominant temporal and convective scales of the flag and of the jet remain close, confirming that the flag behaves as a selective structural filter of the turbulent forcing imposed by the meandering jet.

References

Allen, J. J., & Smits, A. J. (2001). Energy harvesting eel. *Journal of Fluids and Structures*, *15*(3–4), 629–640. doi: 10.1006/jfls.2000.0355

Argentina, M., & Mahadevan, L. (2005). Fluid-flow-induced flutter of a flag. *Proceedings of the National Academy of Sciences*, *102*(6), 1829–1834. doi: 10.1073/pnas.0408383102

Chang, Y. B., & Moretti, P. M. (2002). Flow-induced vibration of free edges of thin films. *Journal of Fluids and Structures*, *16*(7), 989–1008. doi: 10.1006/jfls.2002.0456

Connell, B. S. H., & Yue, D. K. P. (2007). Flapping dynamics of a flag in a uniform stream. *Journal of Fluid Mechanics*, *581*, 33–67. doi: 10.1017/S0022112007005307

Eloy, C., Lagrange, R., Souilliez, C., & Schouveiler, L. (2008). Aeroelastic instability of cantilevered flexible plates in uniform flow. *Journal of Fluid Mechanics*, *611*, 97–106. doi: 10.1017/S002211200800284X

Eloy, C., Souilliez, C., & Schouveiler, L. (2007). Flutter of a rectangular plate. *Journal of Fluids and Structures*, *23*(6), 904–919. doi: 10.1016/j.jfluidstructs.2007.02.002

Miozzi, M., & Romano, G. P. (2020). Propagation of perturbations and meandering in a free surface shallow water jet. *Experiments in Fluids*, *61*(9), 1–18. doi: 10.1007/s00348-020-03025-2

Moscato, G., & Romano, G. P. (2023). A comparative study of circular and rectangular bended plunging jets. *Experimental Thermal and Fluid Science*, *145*, 110888. doi: 10.1016/j.expthermflusci .2023.110888

Shelley, M., Vandenberghe, N., & Zhang, J. (2005). Heavy flags undergo spontaneous oscillations in flowing water. *Physical Review Letters*, *94*(9), 094302. doi: 10.1103/PhysRevLett.94.094302

Sollevanti, M., Miozzi, M., & Romano, G. P. (2025). Coandà effect in free-surface shallow-water offset jets. *Experiments in Fluids*, *66*(3), 57. doi: 10.1007/s00348-024-03892-z

Taneda, S. (1968). Waving motions of flags. *Journal of the Physical Society of Japan*, *24*(2), 392–401. doi: 10.1143/JPSJ.24.392

Thielicke, W., & Stamhuis, E. J. (2014). PIVlab: Towards user-friendly, affordable and accurate digital particle image velocimetry in MATLAB. *Journal of Open Research Software*, *2*(1), e30. doi: 10.5334/jors.bl

Wang, Y., Liu, X., Chen, T., Wang, H., Zhu, C., Yu, H., … Xu, M. (2021). An underwater flag-like triboelectric nanogenerator for harvesting ocean current energy under extremely low velocity condition. *Nano Energy*, *90*, 106503. doi: 10.1016/j.nanoen.2021.106503

Watanabe, Y., Suzuki, S., Sugihara, M., & Sueoka, Y. (2002). An experimental study of paper flutter. *Journal of Fluids and Structures*, *16*(4), 529–542. doi: 10.1006/jfls.2001.0435

Zhang, J., Childress, S., Libchaber, A., & Shelley, M. (2000). Flexible filaments in a flowing soap film as a model for one-dimensional flags in a two-dimensional wind. *Nature*, *408*(6814), 835–839. doi: 10.1038/35048530